

Article

# Thickness Dependence of Toughness in Ultra-Heavy Low-Alloyed Steel Plate after Quenching and Tempering

Huibin Liu <sup>1,2</sup>, Hanqian Zhang <sup>1,2</sup> and Jinfu Li <sup>1,\*</sup>

<sup>1</sup> School of Materials Science and Engineering, Shanghai Jiao Tong University, Shanghai 200240, China; liuhuibin@baosteel.com (H.L.); hq\_zhang@baosteel.com (H.Z.)

<sup>2</sup> Baosteel Research Institute, Shanghai 201900, China

\* Correspondence: jfli@sjtu.edu.cn; Tel.: +86-21-5474-8530

Received: 4 July 2018; Accepted: 3 August 2018; Published: 10 August 2018



**Abstract:** Due to the limitations of manufacturing techniques, inhomogeneous microstructures and properties along the thickness direction have been a big challenge for heavy and ultra-heavy plates of quenched and tempered low-alloyed steel. In this study, variation in microstructures and mechanical properties were investigated from the surface to the center of a 130 mm-thick ultra-heavy steel plate. Emphasis was made on toughness performance including impact toughness and crack resisting ability. It was found that the ultimate tensile strength at the plate surface, quarter and center thickness at room temperature are 715, 643 and 618 MPa, respectively. Meanwhile, the ductile-brittle transition temperature defined by fracture appearance for these three plate positions are  $-100$ ,  $-30$  and  $-15$  °C, respectively. Moreover, the crack resisting ability represented by the nil-ductility temperature are  $-40$ ,  $-25$  and  $-10$  °C for these three positions respectively. Investigation by field emission scanning electron microscopy (FE-SEM) and electron backscatter diffraction (EBSD) revealed that the plate surface features finer matrix grain and carbide precipitation, as well as greater frequency of high angle misorientation. These microstructural features contribute to enhancing deformability, retarding cleavage initiation and hindering crack propagation, leading to the pronounced increase in the energy for fracture propagation and the overall impact energy as compared to the other two plate positions.

**Keywords:** ultra-heavy steel plate; toughness; instrumented impact; fracture propagation; electron backscatter diffraction

## 1. Introduction

In the last decades, tremendous success has been achieved in the development and application of thermo-mechanically controlled process (TMCP) and millions of tons of steel products with excellent properties are manufactured through this technology each year [1]. The maximum thickness, however, of the steel plates that can be produced from this technology is still limited [2]. On the other hand, heavy and ultra-heavy steel plates (thickness from 50 mm to 200 mm or even greater) are essential in many industrial sections such as nuclear, hydropower, offshore and so on [3,4]. With the improvement of heat treatment technology in steel mills, these heavy steel plates can at present be manufactured through heat treatment including normalizing, quenching and tempering. Among them, quenching and tempering has the advantage of achieving higher strength together with better toughness compared with other treatments [3,4].

During the quenching process, heat from the inner part of ultra-heavy plates can only be gradually transferred away through the outer part of the plates and thus the cooling rate cannot be very high. At the same time, modern quenched and tempered steels face the restriction of limited use of carbon content and/or alloying contents (represented by carbon equivalent value as a whole) because of the

customers' concern on weldability, which hinders the alloy design from being hardenable enough [5]. The combined consequence is the inhomogeneity in microstructure distributed through the plate thickness. A small portion beneath the plate surface is exposed to fast cooling and low-temperature transformation products such as martensite and lath bainite form, while relatively slow cooling rates in the inner section of the heavy plate produces high-temperature transformation products like granular bainite or even ferrite.

An inhomogeneous microstructure is usually considered undesirable as it may lead to property fluctuation and scattering and affect ultimate service performance; however, the effect of microstructural inhomogeneity of this kind, through the thickness direction of ultra-heavy steel plate on property performance, is still unclear [5]. Although some work has been done on the difference in microstructure as well as properties of ultra-heavy steel plate, they tended to employ simulated lab samples rather than ultra-heavy plate itself [4,6]. The aim of this study is to investigate accurately the thickness-dependent properties in a practical low-alloyed ultra-heavy steel plate manufactured by quenching and tempering and the correlations with microstructural features, so that a reliable conclusion can be made on the consequence of such inhomogeneous microstructure on the steel's performance.

## 2. Materials and Methods

The ultra-heavy steel plate was manufactured by Baosteel (Shanghai, China). Steelmaking was carried out by an industrial scale converter and secondary refining and the steel's composition is shown in Table 1. 130 mm-thick plate was obtained through rolling of the cast ingot in a 5 m-wide rolling machine. The rolled plate was austenitised at 900 °C for 280 min, followed by water quenching to room temperature and then tempered at 630 °C for 360 min. Both quenching and tempering were conducted continuously in a roller hearth furnace (LOI, Essen, Germany).

**Table 1.** Chemical composition of SA738Gr.B steel plates (wt %, Fe: bal.).

C	Si	Mn	P	S	Cu + Ni + Cr	Mo	V + Nb
0.088	0.22	1.40	0.009	0.0002	0.63	0.27	0.060

Specimens for various mechanical tests were cut from the 130 mm-thick plate at different thickness positions. Round tensile specimens with a gauge diameter of 10 mm and a gauge length of 50 mm were prepared in the transverse direction of rolling and were tested from −80 °C to room temperature at a strain rate of  $4.76 \times 10^{-4} \text{ s}^{-1}$  using a 100 kN MTS machine (Company, City, Country) in accordance with ASTM E8. An extensometer (MTS, MN, USA) was attached to the gauge section of the specimens for measuring displacement. Charpy impact bars with a  $10 \times 10 \text{ mm}^2$  section and a 2 mm-deep V-notch were machined in the transverse-longitudinal (T-L) orientation. The tests were carried out according to ASTM E23 using a Zwick PSW IWI testing machine with 750 J capacity in the temperature range from −100 °C to room temperature. Load-displacement curves of impact tests at −20 °C were recorded from the instrumented Charpy impact system attached into the impact tester. Two types of Pellini drop weight specimens were prepared: P-2 and P-3, which are only different in their thickness—16 mm and 20 mm respectively. For each specimen, a crack starter weld-bead was deposited in a single pass using D127 coated electrodes with diameter of 4 mm. This is a brittle weld bead that can initiate crack quickly as the drop hammer begins to contact the other side of sample and enforce deformation under three-point bend. The deposition procedure was carried out according to standard requirements of ASTM E208. The tests were carried out in a SANS ZJC2602 machine (Shenzhen, China) with hammer energy of 405 J at temperature ranged from −100 to 0 °C. For all the tensile, impact and drop weight tests, specimens cut from three different locations along the plate thickness were prepared and tested. The specimens that were sampled just beneath the plate surface were denoted as 0 t. The others with longitudinal axes that coincide with the quarter and center of plate thickness were denoted as 1/4 t and

1/2 t respectively. 0 t, 1/4 t and 1/2 t sometimes also denote the position of the surface, 1/4 thickness and 1/2 thickness of the steel plate. Samples for various mechanical tests and their positions in the plate section are schematically shown in Figure 1.

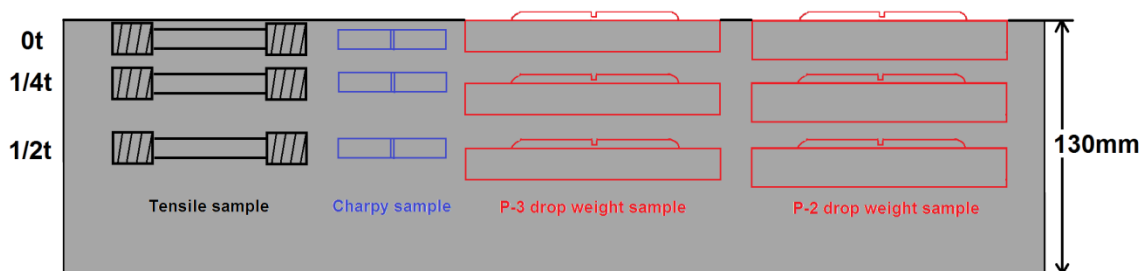


**Figure 1.** Schematic diagram of mechanical samples and the corresponding position in the plate section.

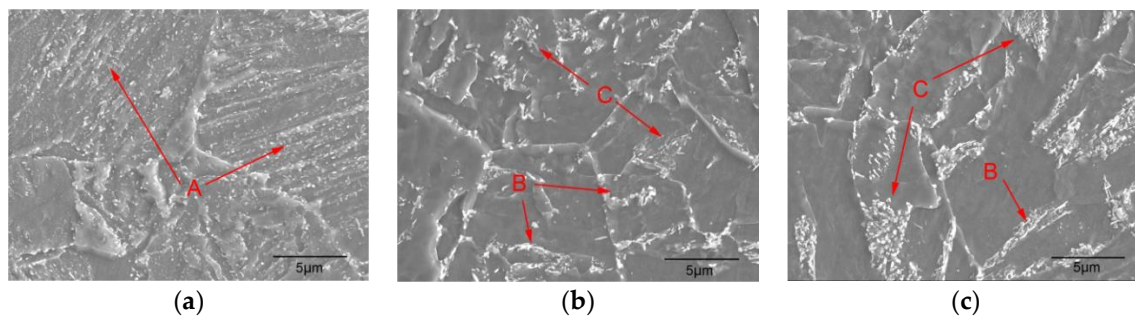
After the test, fracture surfaces and cross-sectional areas of the Charpy impact specimens were examined using a scanning electronic microscope (SEM) to observe fracture modes and fracture initiation and propagation paths. The microstructures were also examined by SEM after etching with 2% Nital. A field emission SEM (JEOL 7000, Tokyo, Japan) equipped with an electron backscattered diffraction (EBSD) system was employed to analyze the information on grain boundaries and misorientation with mechanically polished samples using colloidal silica (Struers, Ballerup, Denmark). The collected EBSD data were analyzed with HKL Channel 5 software (Oxford Instruments, High Wycombe, UK).

### 3. Results

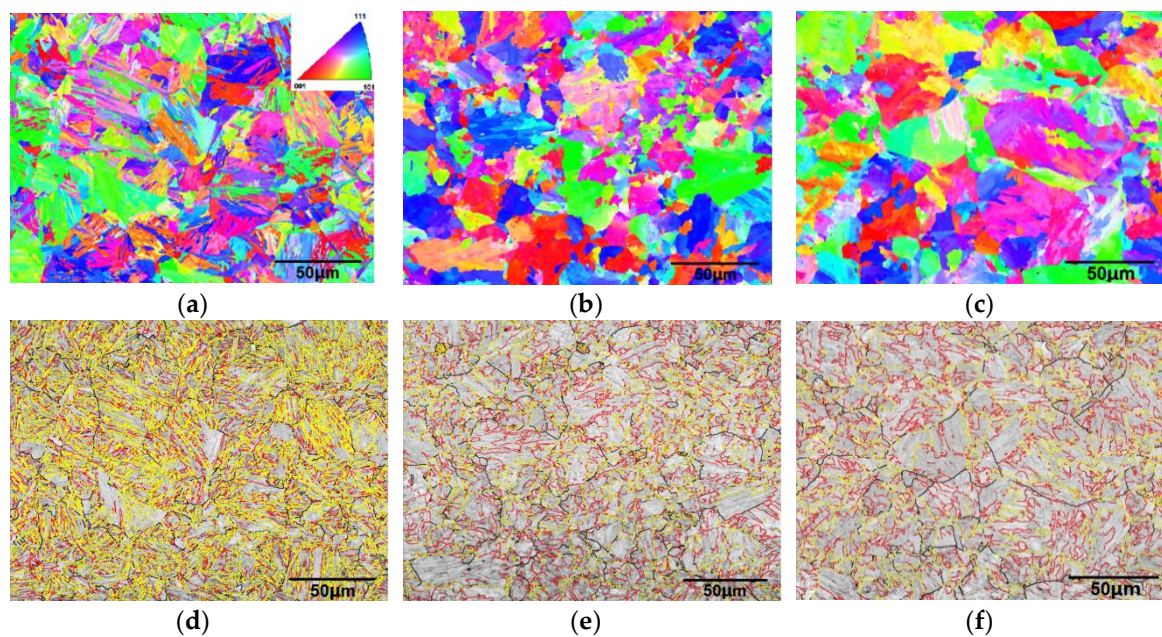
#### 3.1. Microstructure

Figure 2 shows the microstructures of 130 mm-thick low-alloyed steel at different thickness positions. It can be seen that the microstructure of 0 t is mainly tempered martensite, with fine carbides precipitating evenly along the grain and lath boundaries. In contrast, the microstructure at 1/4 t consists of bainite, with carbides aggregating in blocks or plates. This bainite has been identified as mainly granular bainite (GB) together with a small portion of lath bainite (LB), which often appear under continuously cooling condition [7]. These blocky or plate-like clusters aggregated with carbides correspond to the Martensite or Austenite (MA) constituents that were originally formed during mediate-rate cooling. Rich in carbon, they decomposed and precipitated carbides during later tempering process. A similar structure was observed at 1/2 t but both matrix grains and carbides blocks are slightly larger than that of 1/4 t due to relatively lower cooling rate during quenching.

EBSD analysis provides more crystal orientation information at three positions. Figure 3a–c are inverse pole figure (IPF) maps in which different colors represent different crystallographic orientations. The horizontal direction in the maps is parallel to the rolling direction of the plate and the vertical direction is parallel to the normal direction of the plate. A grain is considered to be a contiguous area of at least 2 pixels surrounded by boundaries of at least  $2^\circ$  misorientation [8]. Consistent with SEM observation, these IPF maps confirm that 0 t is characterized with tiny lath-shaped structure, while 1/4 t and 1/2 t exhibit similar feature of mainly equiaxed grains, with some obscure lath features appearing in some areas. Figure 3d–f are grain boundary maps in which boundaries are divided into three groups based on degree of misorientation. Between 2 and 15 degrees (red lines) are low angle boundaries existing between laths within a common block; between 15 and 45 degrees (yellow lines) are attributed to prior austenite grain boundaries; and greater than 45 degrees (black lines) refers mainly to boundaries between blocks and packets [9]. The most obvious result is that the density of high angle grain boundary (greater than 45 degree) is much larger in 0 t position than in the other two positions.



**Figure 2.** Scanning electron microscope (SEM) microstructural images of 130 mm-thick steel plate. (a) 0 t; (b) 1/4 t; (c) 1/2 t. A denotes carbides precipitating on lath boundaries; B and C denote lath-like and blocky colonies of carbides respectively.



**Figure 3.** IPF (inverse pole figure) maps (a–c) and the corresponding boundary maps (d–f) (red line:  $2^\circ < \theta < 15^\circ$ , black line:  $15^\circ < \theta < 45^\circ$ , yellow line:  $\theta > 45^\circ$ ) of a 130 mm-thick steel plate. (a,d) 0 t; (b,e) 1/4 t; (c,f) 1/2 t.

### 3.2. Tensile Properties

Two samples at each testing temperature were tested and the average value of results are plotted against temperature in Figure 4a. The difference in strength (including higher ultimate tensile strength (UTS) and yield strength (YS)) between two samples at each point ranges from 0 to 15 MPa. It is evident that in all cases the strength decreases with increasing testing temperature due to the decreased Peierls-Nabarro resistance stress to dislocation movement at higher temperatures, which is common in a bcc lattice [10]. Specifically, the 0 t exhibits the largest strength, followed by the 1/4 t and then the 1/2 t. Additionally, the UTS increases slightly faster than YS with decreasing temperature due to the higher strain hardening rate as temperature goes down. Figure 4b illustrates the corresponding ductility represented by elongation after fracture and reduction of area. The reduction of area increases with the increasing temperature and decreasing strength at a whole but the elongation after fracture slightly decreases with temperature.

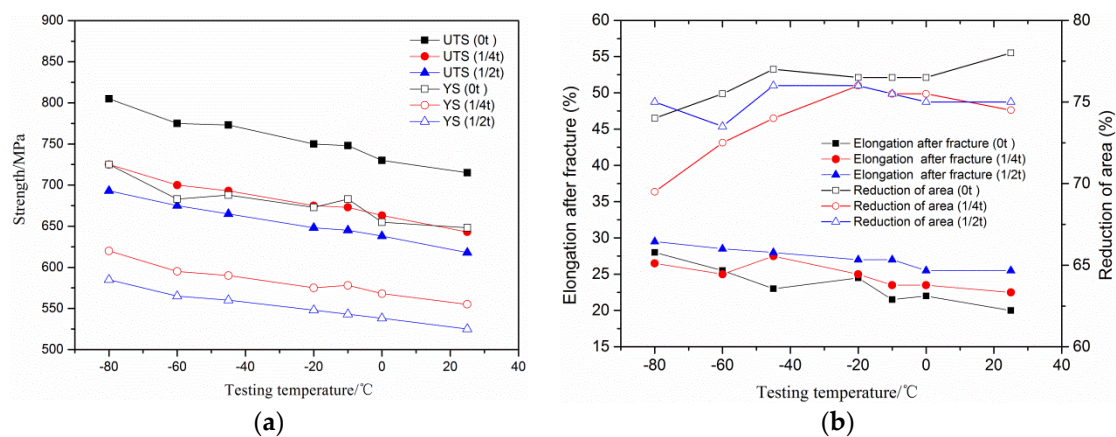


**Figure 4.** Tensile properties of 130 mm-thick steel plate at various temperatures. (a) ultimate tensile strength (UST) and yield strength (YS); (b) elongation after fracture and reduction of area.

### 3.3. Impact Toughness

The testing results of Charpy V-notch impact are shown in Figure 5. It can be seen that, the variation of impact energy across the thickness of the 130 mm-thick plate is manifest over most of the testing temperature range. The toughness of 0 t is superior to those of 1/4 t and 1/2 t and does not fully reach the lower shelf even at  $-100$  °C. The 1/2 t has the lowest impact toughness among the three thickness positions.

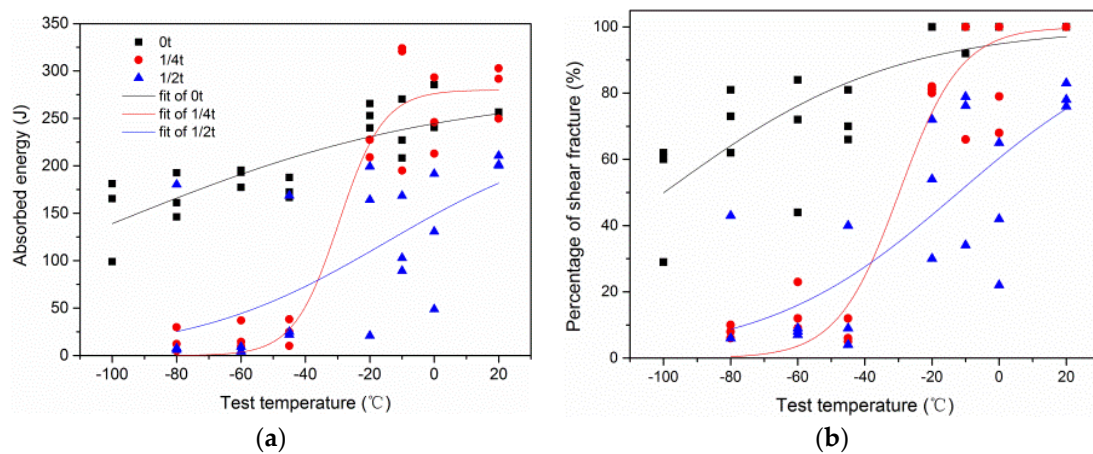


**Figure 5.** Ductile-brittle transition determined by Charpy impact tests of 130 mm-thick plates. (a) absorbed energy; (b) percentage of shear fracture.

The hyperbolic tangent fitting has been extensively used for ductile-brittle transition (DBT) of impact toughness [11]. The fitted curves using this method are depicted for absorbed energy (a) and shear-fracture percentage (b). Only the fitted curve for 1/4 t exhibits complete DBT shape from upper shelf to lower shelf in the testing temperature range of the present study. 0 t does not reach its lower shelf as low as  $-100$  °C, while the upper shelf of 1/2 t appears to be above  $20$  °C. From the curves, the index parameters, such as upper-shelf energy (USE), temperature corresponding to impact energy of 68 J and lateral expansion of 0.89 mm ( $T_{68J}$  and  $T_{0.89mm}$ ), fracture appearance transition temperature (FATT) were determined and the values are shown in Table 2. These indicators are often exploited to evaluate material toughness in industry.

The remarkable toughness variation in the 130 mm-thick plate is due to the relatively large cooling rate difference from plate surface to center during quenching, which is inherent for quenched

and tempered ultra-heavy plates. A slower cooling rate results in both coarser precipitation and appearance of ferrite, which are detrimental to crack initiation and propagation respectively and the overall toughness.

**Table 2.** Results of Charpy impact and Pellini drop weight tests.

Thickness Position	Impact Toughness			$T_{NDT}$ (°C)		
	USE (J)	$T_{68J}$ (°C)	$T_{0.89mm}$ (°C)	FATT (°C)	P-2	P-3
0 t	271	<−100	<−100	−100	−40	−40
1/4 t	287	−38	−37	−30	−25	−25
1/2 t	211	−43	−46	−15	−10	−5

In addition, ferrite steels with BCC structure tend to display scatter in toughness in the ductile-brittle transition range, which can be seen in Figure 5. The probability of finding potential cleavage initiation sites such as inclusions or large carbides at the maximum stress position in front of the notch is an important reason for toughness scattering. In this study, care has been taken on the preparation and testing of impact samples to maintain uniformity, therefore the scatter is believed to be due to microstructural reason(s). But detailed investigation is needed in the future.

### 3.4. Instrumented Charpy Impact

Generally, the impact absorbed energy can be divided into two parts: the energy needed for fracture initiation and that for fracture propagation. In order to elucidate the difference of impact toughness among three thickness positions in more details, instrumented impact tests were utilized to separate toughness between these two processes. The load-displace curves during impact process at  $-20$  °C are shown in Figure 6. It can be seen that these curves illustrate the typical features of ductile-brittle transition in impact loading. Load first linearly increases with displacement until the general yield point; then load changes to increase parabolically with increasing displacement until a maximum load is achieved; after that load begins to decrease slowly which is interrupted by a sudden drop with little increase in displacement; at a certain load level the vertical drop is arrested and the displacement begins to increase again till load approaches zero.

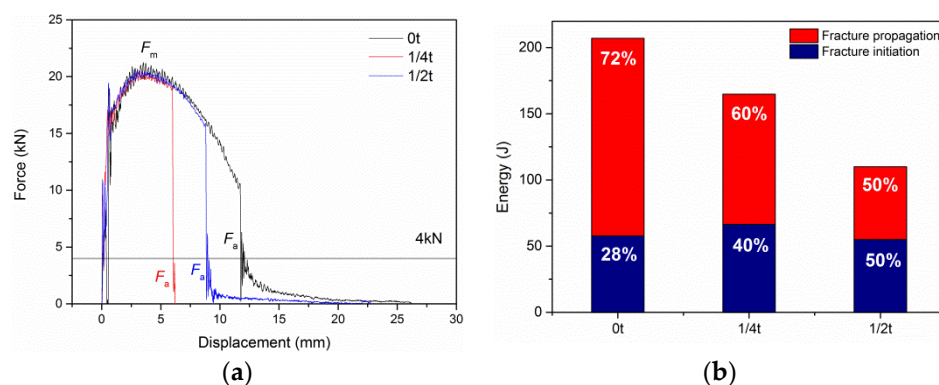


**Figure 6.** (a) Load versus displacement plot of 130 mm-thick steel plate obtained by instrumented impact at  $-20$  °C. The point of crack initiation is indicated by  $F_m$  and the point of crack arrest is indicated by  $F_a$ . (b) Fracture initiation and propagation energy at  $-20$  °C obtained from load-displacement curves of the instrumented Charpy impact tests.

Though different methods were used to quantify the fracture initiation energy in the instrumented impact curve [12–14], the energy corresponding to the maximum load is related with the crack initiation and has been used most [15]. So, it is also used in this work as an indicator of fracture initiation energy.

The energy corresponding to maximum force in 0 t, 1/4 t and 1/2 t are 58, 67 and 55 J respectively, composing 28%, 40%, 50% of the over energy respectively, as shown in Figure 6b.

The fracture propagation energy in Charpy impact tests was determined by the remnant of total absorbed energy subtracting the part corresponding to maximum load, that is,  $W-W_m$ . In spite of the similar fracture initiation energy among three thickness positions, their propagation part displays obvious differences, as can be seen in Figure 6. The 0 t has largest fracture propagation energy of 149 J, followed by 98 J of 1/4 t and 55 J of 1/2 t.

The load-displace curves also provide information on crack-resistance ability, which is also an important toughness indicator. Some researchers have established that the arrest load,  $F_a$ , which corresponds to the end of unstable crack propagation, is a good indicator of crack arrest temperature when its value equals 4 kN [14,16]. Judging from the load-displacement curves at  $-20\text{ }^\circ\text{C}$  shown in Figure 6a, values of  $F_a$  at 0 t, 1/4 t and 1/2 t are above, close to and below 4 kN, respectively, suggesting that their crack resisting temperatures are above, close to and below  $-20\text{ }^\circ\text{C}$ , respectively.

### 3.5. Pellini Drop Weight Tests

The toughness performances of the materials at three positions were also evaluated by the Pellini drop weight tests, which was invented and applied successfully to quenched and tempered steel plates [17]. For this specimen, a notch is machined in the brittle weld metal deposited on the surface. When the hammer begins to contact the opposite side of the weld bead, a crack will initiate easily first in the brittle weld-bead notch with very little energy requirement and then propagate into the base metal [18]. Therefore, the extent to which a crack can develop within the base metal depends mainly on its ability to resist crack propagation. It has been demonstrated that the nil-ductility temperature obtained through Pellini drop weight tests is a good indicator of a material's crack-arresting ability [17]. Compared to the scatter in impact energy values, the results of the Pellini drop weight tests are quite stable and the nil-ductility temperature is within  $\pm 5\text{ }^\circ\text{C}$  [17], which is also confirmed in our study.

The nil-ductility temperature ( $T_{\text{NDT}}$ ) determined is listed in Table 2. The 0 t has the lowest  $T_{\text{NDT}}$  and 1/2 t the highest, with 1/4 t in the middle, indicating the resistance of fracture propagation decreases gradually from the plate surface to the center. Additionally, these results of  $T_{\text{NDT}}$  are well consistent with the crack-arresting results provided by instrumented impact tests as analyzed in Section 3.4. The 16 mm-thick P-3 specimens exhibit the same nil-ductility temperature ( $T_{\text{NDT}}$ ) with the 20 mm-thick P-2 specimens at 0 t and 1/4 t positions but  $5\text{ }^\circ\text{C}$  lower at 1/2 t position, probably due to the thickness-caused decrease in plastic constraint during deformation and fracture.

## 4. Discussion

For the Charpy impact test, the 2 mm-deep and  $45^\circ$  notch introduces a triaxial stress state in the sample, which intensifies stress and restricts plastic deformation [10]. The failure process starts with a crack initiating from non-metallic inclusions or carbides beneath the notch, then propagating into adjacent ferrite grain and finally developing into macroscopic crack [19]. For ferritic steels in the ductile-brittle transition zone, cleavage crack initiation is preceded by plastic deformation, the extent of which depends on the ease of cleavage crack initiation. So, the competition between plastic deformation and crack initiation has a significant effect on when the unstable fracture happens, which dominates most of the energy absorbed by the impact sample. The cleavage initiation site in ferritic steels have been identified previously as carbides, non-metallic inclusions, MA constitutes and so forth, in different situations [20–22]. Inclusions may not be as important here as found in previous studies [22] since both the size and density have been greatly reduced thanks to modern steelmaking process, evidenced by the sulfur content being lower than 0.001%. But it is evident that the carbides in tempered martensite at 0 t are smaller than that in tempered bainite in 1/4 t and 1/2 t, similar with the results of other studies [21], indicating a lower possibility of cleavage initiation. As a result, the cleavage crack initiation becomes much more difficult as initiation sites of carbides and non-metallic inclusions were reduced in both size and number. Therefore, considerable deformation

happens before crack initiation, which is implied by the FATT and  $T_{0.89}$  mm listed in Table 2 and thus contributed greatly to the impact toughness. Moreover, the clusters of carbides appearing in 1/4 t and 1/2 t may also be potential cleavage initiation sites, as discovered by some researchers [20], as their size are larger than the single carbide. This means that there is a higher chance of initiating cleavage cracks compared with the 0 t sample, besides the difference in carbide size. The possibility at 1/2 t should be greater than 1/4 t since the carbide blocks are coarser. These microstructural features result in the early development of cleavage fracture during impact loading and reduce the overall energy remarkably, as shown in Figure 6.

The other important factor affecting the toughness is the ease of crack propagation after it has been initiated by imposed stress at low temperatures. In other words, the material with greater crack resistant ability will have better toughness than that lacking such ability. It has been well known that high angle boundaries are effective barriers to crack propagation and cracks tend to be deflected or even arrested at such boundaries. The more cracks are deflected or arrested, the more energy the sample consumes till fracture. Since the densities of misorientation at the three positions of the present ultra-thick steel plate have significant discrepancy as shown in Figure 3, it is expected that they should be quite different in ability of resisting crack propagation. Their misorientation distribution with angle is quantitatively compared in Figure 7. Though 0 t has a lower ratio of boundary at misorientation angle below  $15^\circ$  compared with 1/4 t and 1/2 t, it has much more pronounced boundaries larger than  $50^\circ$ , with a sharp peak appearing at around  $60^\circ$ . It should be pointed out that this misorientation may not be perfect, since the EBSD step size of about  $0.3 \mu\text{m}$  was selected in this study, and some microstructural features—for example the longitudinal length of a portion of the largest carbides—are similar in size to this step size and this may affect the exact result of misorientation.

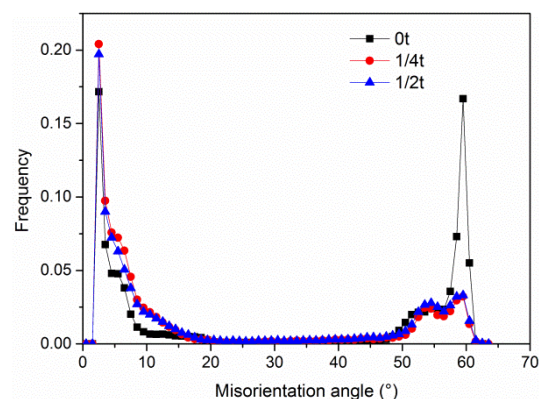
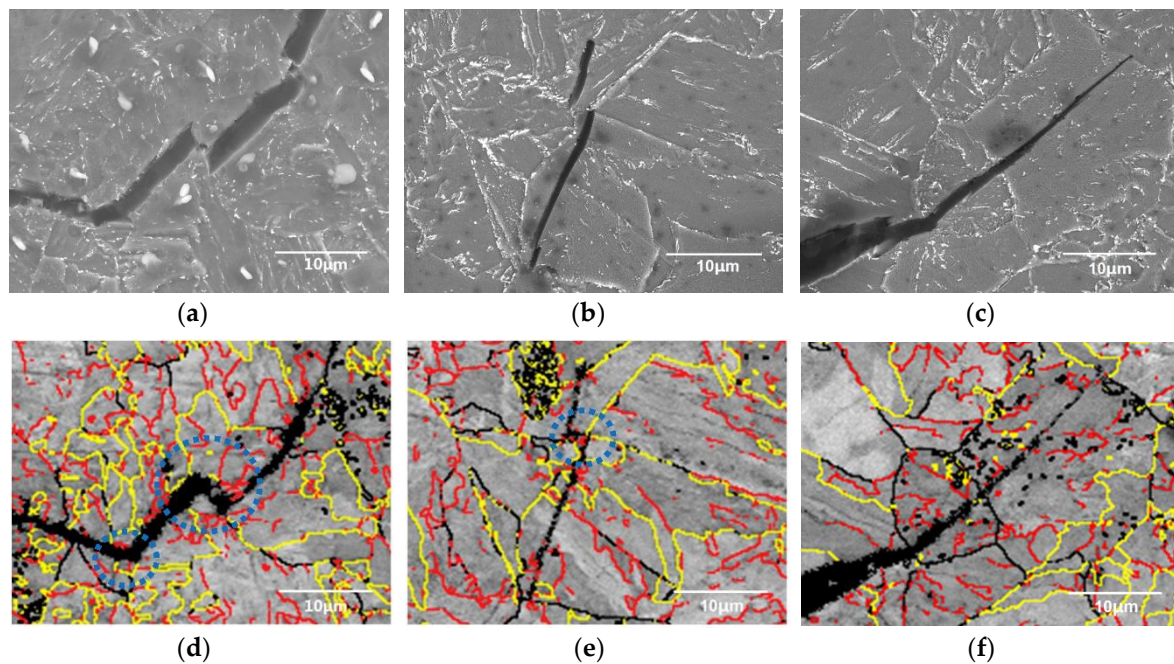


Figure 7. Frequency of grain boundaries at three positions.

To investigate the crack propagation interaction with the feature of grain boundaries, the secondary cracks seen on the cross-sections of the fractured impact specimens were examined. Shown in Figure 8a–c are representative SEM images of the secondary cracks and (d–f) are the corresponding band contrast maps plus grain boundaries with different misorientations. It can be clearly seen that all secondary cracks are transgranular. But the crack at 0 t was much more tortuous than those in the other two positions. High angle boundaries greater than  $45^\circ$  were always observed at the positions where cracks were deflected which agrees well with the literature [7,9]. Moreover, when coming across misorientation greater than  $45^\circ$  the secondary crack is not only deflected but shows a zig-zag pattern, as denoted by blue dashed circles in Figure 8d–f. In contrast, cracks at 1/4 t and 1/2 t are quite straight with few high-degree boundaries present on their moving path. After the motion energy of the cleavage crack was gradually diminished to a certain extent by the high angle boundaries on its moving path, they tended to be finally arrested on high angle boundaries.



**Figure 8.** SEM (a–c) and boundary images (d–f) (red line:  $2^\circ < \theta < 15^\circ$ , black line:  $15^\circ < \theta < 45^\circ$ , yellow line:  $\theta > 45^\circ$ ) of the secondary cracks observed on the fractured V-notch Charpy sample at  $-20^\circ\text{C}$ . (a,d) 0 t; (b,e) 1/4 t; (c,f) 1/2 t.

Results of the fractography investigation by SEM are presented in Figure 9. The unstable fracture surface is transgranular and consists of quasi-cleavage and microvoids. The cleavage initiation sites at 1/4 t and 1/2 t are found to be at non-metallic inclusions. But no inclusions were observed in the initiation sites of 0 t. Nor were other microstructural features such as carbides and MA constituents which are usually considered to initiate cleavage. The cleavage facet size varies, with 0 t being the smallest, 1/4 t the second and 1/2 t the largest, which is similar to the grain size analysis by EBSD. Secondary cracks are also present as the unstable fracture propagates with transgranular features (Figure 9d–f). They are also transgranular. While secondary cracks of 0 t are tortuous, those of 1/4 t and 1/2 t tend to be straight.

Besides toughness, the high frequency of grain boundaries also contributes to strength. Generally, the Hall-Petch relationship describes how strength increases with decreasing grain size, that is, higher grain boundary density. Specifically in martensite or bainite with lath morphology, some researchers discovered that the increase in strength with grain size followed a reciprocal correlation rather than Hall-Petch relationship [23,24]. This is because the stress concentration is hardly achieved inside the very thin lath. Since the laths inside a block or packet are divided by low angle boundaries, the strength is related with the grains divided by small misorientations. Recent research also found that the strength of low-alloyed steel correlated well with the grain size calculation based on low angle grain boundaries such as  $2\text{--}6^\circ$  [25]. Here we calculated the equivalent grain size of three positions based on different small orientations no greater than  $15^\circ$ . The greater the critical misorientation that was chosen, the larger the grain size [25]. For example, if  $5^\circ$  is chosen as the critical misorientation, the grain size at 0 t, 1/4 t and 1/2 t were determined as 0.81, 1.98 and 2.46  $\mu\text{m}$  respectively.

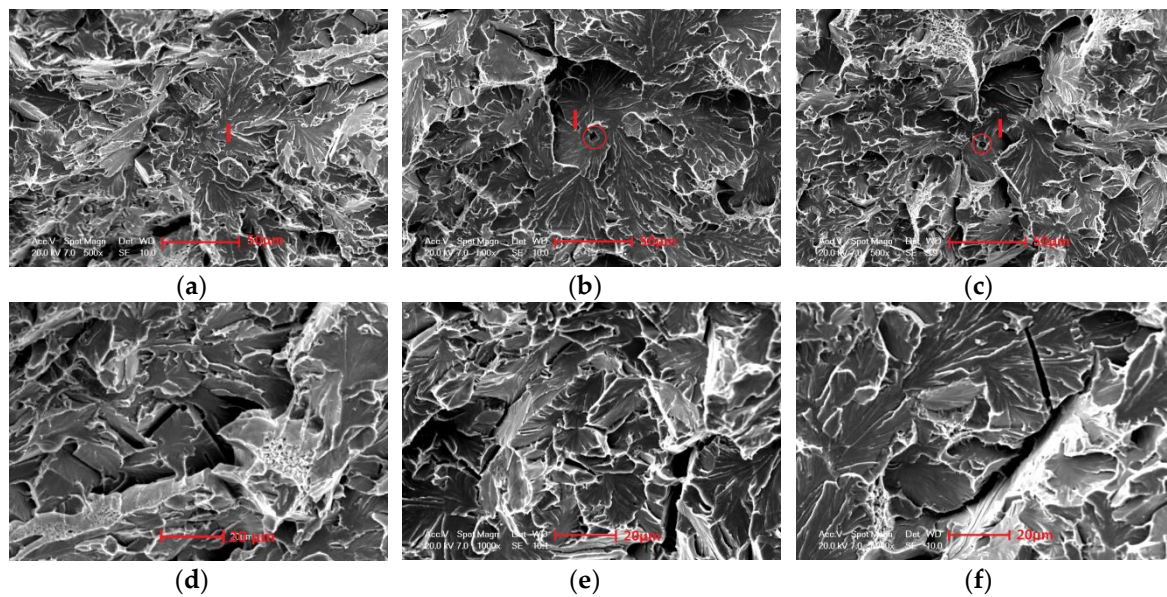


**Figure 9.** SEM fractography of impact specimens. (a,d) 0 t; (b,e) 1/4 t; (c,f) 1/2 t. Cleavage initiation sites are denoted as I; inclusions are denoted by red circles.

## 5. Conclusions

The 130 mm-thick low-alloyed steel plates manufactured through quenching and tempering was examined in terms of inhomogeneity in properties and microstructures. It is found that the plate surface (0 t) has higher ultimate tensile strength (UTS) of 715 MPa than quarter thickness (1/4 t) of 643 MPa and center thickness (1/2 t) of 618 MPa at room temperature. Moreover, the best toughness represented by 50% fracture appearance transition temperature (*FATT*) of  $-100$  °C and nil-ductility temperature ( $T_{NDT}$ ) are also discovered in the plate surface (0 t), while quarter thickness (1/4 t) and center thickness (1/2 t) have *FATT* of  $-30$  and  $-15$  °C,  $T_{NDT}$  of  $-25$  and  $-10$  °C, respectively. The superior toughness performance at the plate surface comes from finer grains (lath), smaller carbides and greater frequency of high angle misorientation, which are beneficial in enhancing deformability, retarding cleavage initiation and hindering crack propagation. Consequently, the energy for fracture propagation and overall impact energy have been significantly improved.

**Author Contributions:** Investigation, H.L.; Writing-Original Draft Preparation, H.L.; Writing-Review & Editing, J.L.; Supervision, H.Z and J.L.; Project Administration, H.Z.

**Funding:** This research received no external funding.

**Acknowledgments:** The authors are grateful for the help with mechanical testing from Jianwei Zhang and for EBSD obtained from Jufeng Hong at Baosteel.

**Conflicts of Interest:** The authors declare no conflict of interest.

## References

1. Buchmayr, B. Thermomechanical Treatment of Steels—A Real Disruptive Technology Since Decades. *Steel Res. Int.* **2017**, *88*, 1700182. [[CrossRef](#)]
2. Tsuyama, S. Thick Plate Technology for the Last 100 Years: A World Leader in Thermo Mechanical Control Process. *ISIJ Int.* **2015**, *55*, 67–78. [[CrossRef](#)]
3. Yen, H.; Chiang, M.; Lin, Y.; Chen, D.; Huang, C.; Lin, H. High-Temperature Tempered Martensite Embrittlement in Quenched-and-Tempered Offshore Steels. *Metals* **2017**, *7*, 253. [[CrossRef](#)]
4. Zhou, T.; Yu, H.; Wang, S. Microstructural Characterization and Mechanical Properties across Thickness of Ultra-Heavy Steel Plate. *Steel Res. Int.* **2017**, *88*, 1700132. [[CrossRef](#)]

5. Hu, J.; Du, L.; Xie, H.; Gao, X.; Misra, R. Microstructure and mechanical properties of TMCP heavy plate microalloyed steel. *Mater. Sci. Eng. A* **2014**, *607*, 122–131. [[CrossRef](#)]
6. Zhou, T.; Yu, H.; Wang, S. Effect of microstructural types on toughness and microstructural optimization of ultra-heavy steel plate: EBSD analysis and microscopic fracture mechanism. *Mater. Sci. Eng. A* **2016**, *658*, 150–158. [[CrossRef](#)]
7. Wang, X.L.; Wang, Z.Q.; Ma, X.P.; Subramanian, S.V.; Xie, Z.J.; Shang, C.J.; Li, X.C. Analysis of impact toughness scatter in simulated coarse-grained HAZ of E550 grade offshore engineering steel from the aspect of crystallographic structure. *Mater. Charact.* **2018**, *140*, 312–319. [[CrossRef](#)]
8. Petrov, R.; Kestens, L.; Wasilkowska, A.; Houbaert, Y. Microstructure and texture of a lightly deformed TRIP-assisted steel characterized by means of the EBSD technique. *Mater. Sci. Eng. A* **2007**, *447*, 285–297. [[CrossRef](#)]
9. Gourgues, A.F.; Flower, H.M.; Lindley, T.C. Electron backscattering diffraction study of acicular ferrite, bainite, and martensite steel microstructures. *Mater. Sci. Technol.* **2000**, *16*, 26–40. [[CrossRef](#)]
10. Dieter, G.E.; Bacon, D.J. *Mechanical Metallurgy*; McGraw-Hill: New York, NY, USA, 1986.
11. Tanguy, B.; Besson, J.; Piques, R.; Pineau, A. Ductile to brittle transition of an A508 steel characterized by Charpy impact test Part I: Experimental results. *Eng. Fract. Mech.* **2005**, *72*, 49–72. [[CrossRef](#)]
12. Tavares, S.S.M.; Silva, M.B.; de Macêdo, M.C.S.; Strohaecker, T.R.; Costa, V.M. Characterization of fracture behavior of a Ti alloyed supermartensitic 12%Cr stainless steel using Charpy instrumented impact tests. *Eng. Fail. Anal.* **2017**, *82*, 695–702. [[CrossRef](#)]
13. Schindler, H.J.; Morf, U. A closer look at estimation of fracture toughness from Charpy V-notch tests. *Int. J. Press. Vessels Pip.* **1993**, *55*, 203–212. [[CrossRef](#)]
14. Chaouadi, R.; Fabry, A. On the utilization of the instrumented Charpy impact test for characterizing the flow and fracture behavior of reactor pressure vessel steels. In *European Structural Integrity Society*; Elsevier: Amsterdam, The Netherlands, 2002; Volume 30, pp. 103–117.
15. Kim, H.; Park, J.; Kang, M.; Lee, S. Interpretation of Charpy impact energy characteristics by microstructural evolution of dynamically compressed specimens in three tempered martensitic steels. *Mater. Sci. Eng. A* **2016**, *649*, 57–67. [[CrossRef](#)]
16. Wallin, K.; Karjalainen-Roikonen, P.; Suikkanen, P. Crack arrest toughness estimation for high strength steels from sub-sized instrumented Charpy-V tests. In *Proceedings of the 26th International Ocean and Polar Engineering Conference*, Rhodes, Greece, 26 June–2 July 2016; pp. 85–91.
17. Wiesner, C.S. Predicting structural crack arrest behaviour using small-scale material characterisation tests. *J. Press. Vessels Pip.* **1996**, *69*, 185–196. [[CrossRef](#)]
18. Hertzberg, R.W. *Deformation and Fracture Mechanics of Engineering Materials*; Wiley: Hoboken, NJ, USA, 1989.
19. Chen, J.; Cao, R. *Micromechanism of Cleavage Fracture of Metals: A Comprehensive Microphysical Model for Cleavage Cracking in Metals*; Butterworth-Heinemann: Oxford, UK, 2014.
20. Zhang, X.Z.; Knott, J.F. Cleavage fracture in bainitic and martensitic microstructures. *Acta Mater.* **1999**, *47*, 3483–3495. [[CrossRef](#)]
21. Bowen, P.; Druce, S.G.; Knott, J.F. Effects of microstructure on cleavage fracture in pressure vessel steel. *Acta Metall.* **1986**, *34*, 1121–1131. [[CrossRef](#)]
22. Filho, W.W.A.B.; Carvalho, A.L.M.A.; Bowen, P.B. Micromechanisms of cleavage fracture initiation from inclusions in ferritic welds. Part I. Quantification of local fracture behaviour observed in notched testpieces. *Mater. Sci. Eng. A* **2007**, *460*, 436–452. [[CrossRef](#)]
23. Naylor, J.P. The influence of the lath morphology on the yield stress and transition temperature of martensitic-bainitic steels. *Metall. Trans. A* **1979**, *10*, 861–873. [[CrossRef](#)]
24. Bush, M.E.; Kelly, P.M. Strengthening mechanisms in bainitic steels. *Acta Metall.* **1971**, *19*, 1363–1371. [[CrossRef](#)]
25. Fan, L.; Zhou, D.; Wang, T.; Li, S.; Wang, Q. Tensile properties of an acicular ferrite and martensite/austenite constituent steel with varying cooling rates. *Mater. Sci. Eng. A* **2014**, *590*, 224–231. [[CrossRef](#)]

